INTERNATIONAL JOURNAL FOR NUMERICAL METHODS IN FLUIDS
Int. J. Numer. Meth. Fluids 2004; **44**:997–1016 (DOI: 10.1002/fld.693)

Interfacial dynamics-based modelling of turbulent cavitating flows, Part-2: Time-dependent computations

Inanc Senocak[‡] and Wei Shyy[*,†]

Department of Mechanical and Aerospace Engineering, University of Florida, Gainesville, FL 32611, U.S.A.

SUMMARY

The interfacial dynamics-based cavitation model, developed in Part-1, is further employed for unsteady flow computations. The pressure-based operator-splitting algorithm (PISO) is extended to handle the time-dependent cavitating flows with particular focus on the coupling of the cavitation and turbulence models, and the large density ratio associated with cavitation. Furthermore, the compressibility effect is important for unsteady cavitating flows because in a water–vapour mixture, depending on the composition, the speed of sound inside the cavity can vary by an order of magnitude. The implications of the issue of the speed of the sound are assessed with alternative modelling approaches. Depending on the geometric confinement of the nozzle, compressibility model and cavitation numbers, either auto-oscillation or quasi-steady behaviour is observed. The adverse pressure gradient in the closure region is stronger at the maximum cavity size. One can also observe that the mass transfer process contributes to the cavitation dynamics. Compared to the steady flow computations, the velocity and vapour volume fraction distributions within the cavity are noticeably improved with time-dependent computations.

KEY WORDS: cavitation; turbulence; unsteady flow; pressure-based method; PISO

1. INTRODUCTION

Different types of cavitation exhibit distinct unsteady characteristics. Sheet cavitation has a quasi-steady character with most of the unsteadiness localized in the closure region. On the other hand, cloud cavitation exhibits strong unsteadiness in the whole cavity [1]. Regarding the origin of the unsteadiness associated with cavitating flows, we briefly mention several recent studies to help describe the current state-of-the-knowledge.

*Correspondence to: Wei Shyy, Department of Mechanical and Aerospace Engineering, University of Florida, 231 Aerospace Building, P.O. BOX 116250, Gainesville, FL 32611, U.S.A.
†E-mail: wss@mae.ufl.edu
‡Present address: Center for Turbulence Research, Stanford University, Building 500, Stanford, CA 94305-3055, U.S.A. E-mail: senocak@stanford.edu

Contract/grant sponsor: NASA URETI Programme
Contract/grant sponsor: U.S. Air Force

Received 29 March 2003
Revised 22 October 2003

Callenaere *et al.* [2] have studied the cavitation instability induced by the development of a re-entrant jet. Two main classes of instabilities have been discussed: intrinsic instabilities and system instabilities. The intrinsic instability originates within the cavity itself, causing the re-entrant jet and the shedding phenomenon. On the other hand, the system instability results from the interaction between the cavity and other components of the hydraulic system such as the flow inlet and outlet lines. It is observed that if the adverse pressure gradient at the closure region of the cavity is strong, then a re-entrant jet develops. The cavity dynamics also depends on the relative thicknesses of the cavity and the re-entrant jet. Watanabe *et al.* [3] and Franc [4] have pointed out that cavitation surge is of a system instability type, for which the dynamic behaviour of the cavity is strongly coupled to its environment. With a one-dimensional model it has been shown that fluctuations in the incoming mass flow rate causes pressure oscillations in the hydraulic system [3]. Duttweiler and Brennen [5] have made detailed experimental investigation of the surge instability on a cavitating propeller in a water tunnel. The instability is observed as the cavitation number becomes sufficiently low. The periodic pressure oscillations resulting from this instability have also been measured away from the cavitating region.

Kubota *et al.* [6] have investigated the unsteady structure of cloud cavitation. The velocity field can be characterized by large- and small-scale structures. The overall cloud cavitation structure is associated with the large-scale velocity, while the small-scale velocity is noticeable around cavity boundaries. Furthermore, the structure of cloud cavitation moves at a velocity smaller than the mean free stream velocity and has a concentrated vorticity region at its centre. Stutz and Reboud [7–9] have experimentally studied the two-phase cavitating flow structure. Both quasi-steady sheet cavitation and large-scale, unsteady cavitation in convergent–divergent nozzles have been examined. The mean values of the void fraction, flow velocity and bubble size inside the cavities have been measured. The unsteadiness of cavitation have been mostly described qualitatively.

Reisman *et al.* [10] have investigated the acoustics of cloud cavitation using piezo-electric pressure transducers and high-speed video camera. Several types of propagating structures, the so-called bubbly shock waves, have been observed. The largest impulsive and radiated noise has been attributed to the coherent collapse of a well-defined separate cloud in regions of high pressure.

On the computational side, recently, substantial efforts have been made in employing the Navier–Stokes equations for turbulent cavitating flows. Both steady and unsteady flow computations have been reported [11–15]. Among the various modelling approaches, the transport equation-based cavitation models have received growing interests [11–15]. In the first part of this study [16], hereinafter referred to as Part-1, we have assessed the merits of alternative transport equation-based modelling approaches. In addition, we have developed an interfacial dynamics-based cavitation model. We have shown that for steady flow computations, all the models considered produce qualitatively comparable pressure distributions. However, quantitative differences have been observed in density and pressure distributions in the closure region of the cavity. For sheet cavitation, satisfactory performance of these models have been established. Furthermore, important flow structures such as vorticity and turbulence production have been probed in Part-1. In spite of good agreement in pressure distributions between different cavitation models, noticeable differences have been observed in the predicted density field. This implies that the compressibility characteristics embodied in each cavitation model are apparently different. This aspect can be significant for unsteady flow computations because

the speed of sound affects the time-dependent features of the cavity. In addition, there are significant computational issues in regard to stability, efficiency and robustness of the numerical algorithm for time-dependent computations of cavitating flows, which involve large density variations between phases, around a factor of 1000 for water, and multiple time scales.

The goals of the present study are as follows:

- Extend the knowledge and experiences gained in our previous research on the pressure-based method for turbulent cavitating flows [14] to unsteady problems, and shed light on important issues in computational modelling of unsteady cavitation.
- Assess the impact of the cavitation model, especially in terms of the compressibility modelling concepts, on predictions of unsteady cavitation.
- Investigate the unsteady cavitation phenomena to gain a better understanding of the fluid physics.

In what follows, the governing equations and the cavitation models are briefly presented. Following this, we present a pressure-based operator-splitting algorithm for time-dependent turbulent cavitating flow computations. The implications of the compressibility effect, reflected via the speed of sound definition, are assessed with two modelling approaches. Cavitating flows in two convergent–divergent nozzles are considered as test problems. The nozzles have different geometric confinement and different degrees of convergent–divergent angles. The computational results are assessed with the time-averaged experimental data from the study of Stutz and Reboud [7–9]. Qualitative descriptions of the unsteady cavitation from various experimental studies are used to support the present findings.

2. GOVERNING EQUATIONS

The set of governing equations consists of the conservative form of the Favre-averaged Navier–Stokes equations plus a transport equation to account for the cavitation dynamics. The equations, written in the Cartesian co-ordinates, are presented as follows:

$$\frac{\partial \bar{\rho}_{\mathrm{m}}}{\partial t} + \nabla \cdot (\bar{\rho}_{\mathrm{m}} \tilde{\mathbf{u}}) = 0 \tag{1}$$

$$\frac{\partial (\bar{\rho}_{\mathrm{m}} \tilde{\boldsymbol{u}})}{\partial t} + \nabla \cdot (\bar{\rho}_{\mathrm{m}} \tilde{\mathbf{u}} \tilde{\mathbf{u}}) = -\nabla \bar{P} + \nabla \cdot (\bar{\tau}_{ij} + \tau_{ij}^{\mathrm{R}}) \tag{2}$$

$$\bar{\tau}_{ij} + \tau_{ij}^{\mathrm{R}} = (\mu + \mu_{\mathrm{t}}) \left[\left(\frac{\partial \tilde{u}_i}{\partial x_j} + \frac{\partial \tilde{u}_j}{\partial x_i} \right) - \frac{2}{3} \delta_{ij} \frac{\partial \tilde{u}_k}{\partial x_k} \right] \tag{3}$$

where P is the pressure, $\boldsymbol{u}$ the velocity vector, ρ_{m} the mixture density, μ the laminar viscosity, μ_{t} the turbulent viscosity, τ_{ij} the viscous stress tensor and τ_{ij}^{R} the Reynolds stresses defined based on the Boussinesq's eddy-viscosity hypothesis. The overbar represents an ensemble-average whereas the tilde represents a density weighted ensemble average.

For cavitation modelling, a transport equation with source terms are solved:

$$\frac{\partial \bar{\alpha}_{\mathrm{L}}}{\partial t} + \nabla \cdot (\bar{\alpha}_{\mathrm{L}} \tilde{\mathbf{u}}) = \dot{m}^{-} + \dot{m}^{+} \tag{4}$$

where α_L is the liquid volume fraction, $\dot{m}^-$ the source term for evaporation and $\dot{m}^+$ the source term for condensation. The mixture density is defined as

$$\bar{\rho}_m = \rho_L \bar{\alpha}_L + \rho_V (1 - \bar{\alpha}_L) \tag{5}$$

where ρ_L and ρ_V are the liquid and vapour densities, respectively. A nominal density ratio of 1000 is assigned. The particular form of the cavitation models are documented in the coming sections. For turbulence closure, the original k–ε model with wall functions is adopted [17, 18]. The present Navier–Stokes solver, documented in References [19, 20], employs pressure-based algorithms and a finite volume approach on collocated multiblock body-fitted curvilinear grids in 2D and 3D domains.

3. INTERFACIAL DYNAMICS-BASED CAVITATION MODEL

In Part-1, we have developed an interfacial dynamics-based cavitation model [16]. The interfacial dynamics-based cavitation model reads as follows:

$$\frac{\partial \bar{\alpha}_L}{\partial t} + \nabla \cdot (\bar{\alpha}_L \tilde{\mathbf{u}}) = \frac{\rho_L \mathrm{MIN}(\bar{P} - P_V, 0)\bar{\alpha}_L}{\rho_V (V_{V,n} - V_{I,n})^2 (\rho_L - \rho_V) t_\infty} + \frac{\mathrm{MAX}(\bar{P} - P_V, 0)(1 - \bar{\alpha}_L)}{(V_{V,n} - V_{I,n})^2 (\rho_L - \rho_V)\, t_\infty} \tag{6}$$

where V is the velocity, P the pressure, $\bar{\alpha}_L$ is the liquid volume fraction, $\boldsymbol{n}$ the normal direction to the interface, ρ the density, $t_\infty = L_{ch}/U_\infty$ the characteristic time scale and L_{ch} and U_∞ are the characteristic length and free stream velocity of the flow problem, respectively. The subscripts I, L, V represent the interface, the liquid phase and the vapour phase, respectively.

For time-dependent computations, the model requires that an interface be constructed in order to compute the interface velocity ($V_{I,n}$), as well as the normal velocity of the vapour phase. For steady flow computations, the interface velocity ($V_{I,n}$) is zero and the normal velocity of the vapour phase can be computed by taking the gradient of the liquid volume fraction [21, 22]. The vapour phase normal velocity is the dot product of the velocity and the normal vector

$$\mathbf{n} = \frac{\nabla \bar{\alpha}_L}{|\nabla \bar{\alpha}_L|} \quad V_{V,n} = \tilde{\mathbf{u}} \cdot \mathbf{n} \tag{7}$$

The derivatives with respect to curvilinear co-ordinates are computed using central differencing of the neighbouring cell-centred nodes. Senocak [15] has provided the details.

The interface velocity is needed for time-dependent problems, and it requires additional methods to track the movement of the interface. In the present effort, the interface velocity is estimated based on a simplified approach, utilizing the mass conservation condition as follows:

$$\rho_L (V_{L,n} - V_{I,n}) = \rho_V (V_{V,n} - V_{I,n}) \tag{8}$$

$$V_{I,n} = \frac{V_{V,n} - (\rho_L/\rho_V)\, V_{L,n}}{1 - (\rho_L/\rho_V)} \tag{9}$$

A single relationship between the liquid-phase normal velocity, ($V_{L,n}$), and the vapour-phase normal velocity, ($V_{V,n}$), is adopted to supply the interface velocity information needed in Equation (6) for time-dependent computations. With this simplification, Equation (9) reads

$$V_{L,n} = f.V_{V,n} \;\Rightarrow\; V_{I,n} = \left[\frac{1 - f\rho_L/\rho_V}{1 - \rho_L/\rho_V}\right] V_{V,n} \tag{10}$$

Specifically, a value of -0.90 is used for f. An estimate of this value can be first extracted from the velocity field and it can be improved through numerical experimentation. Rajkumar *et al.* [23] have presented a systematic evaluation and sensitivity analysis of the empirical parameters of a transport equation-based cavitation model. They have concluded that the empirical constants of the cavitation model, determined through numerical experimentation, are appropriate for different flow conditions. In a more rigorous approach, the interface velocity should be computed based on the mass and momentum exchange in accordance with the interfacial dynamics [24]. However, such computations require additional treatments of the interface movement of turbulent two-phase flows, which need to be further developed and deserve a separate study.

In Part-1 [16], we have shown that different density profiles are yielded by different cavitation models, implying different compressibility characteristics. To investigate this issue in more depth, a second cavitation model [13] is also considered in addition to the newly developed interfacial dynamics-based cavitation model [16]. In Part-1 [16], we have referred to the cavitation model presented below as Model-2. We keep the same model name in the present study as well.

$$\frac{\partial \bar{\alpha}_L}{\partial t} + \nabla \cdot (\bar{\alpha}_L \tilde{\mathbf{u}}) = \frac{C_{dest}\rho_V \,\mathrm{MIN}(\bar{P} - P_V, 0)\bar{\alpha}_L}{(0.50\rho_L U_\infty^2)\rho_L\, t_\infty} + \frac{C_{prod}\bar{\alpha}_L^2(1 - \bar{\alpha}_L)}{\rho_L\, t_\infty} \tag{11}$$

The empirical factors in the above model have the following values, ($C_{dest} = 9.0 \times 10^5$, $C_{prod} = 3.0 \times 10^4$), which have been tuned previously [14].

4. PRESSURE-BASED OPERATOR-SPLITTING ALGORITHM FOR TURBULENT CAVITATING FLOW COMPUTATIONS

In SIMPLE type of pressure-based methods [25], the partial differential equations are solved successively by employing iterations. Such an iterative process for time-dependent computations can be highly expensive. Issa [26] has developed a pressure-based algorithm called the pressure-implicit with splitting of operators (PISO) for the solution of unsteady flows. For steady-state flow computations, this algorithm is similar to the SIMPLER algorithm [27]. The PISO algorithm employs the splitting of operations in the solution of the implicitly discretized momentum and pressure or pressure-correction equations.

Issa [26] has presented the compressible formulation of PISO. In this formulation, the pressure–density coupling is introduced only through the time-dependent term of the continuity equation. Bressloff [28] has extended the PISO algorithm for high-speed flows by adopting the pressure–density coupling procedure.

In the present effort, we extend the PISO algorithm, formulated in Thakur *et al.* [29] for curvilinear co-ordinates with all-speed treatment, for unsteady cavitating flow computations.

The formulation of the present algorithm shares similar features of the formulation presented in Reference [30].

Basically, the discretized momentum equations can be written as

$$A_P^{\mathbf{u}}\mathbf{u}_P = \sum A_{nb}^{\mathbf{u}}\mathbf{u}_{nb} - V_P(\nabla_{\mathrm{d}}P)_P + b_P^{\mathbf{u}} + \frac{(\rho\mathbf{u})^{n-1}}{\delta t} \tag{12}$$

where $A_P^{\boldsymbol{u}}$ and $A_{nb}^{\boldsymbol{u}}$ are the coefficients of the cell centre and neighbouring nodes, respectively, due to the contributions from convection and diffusion terms. V_P and $b_P^{\boldsymbol{u}}$ represent the volume of the cell and the source term, respectively. Note that the ∇_{d} operator is the discrete form of the gradient operator.

In the predictor step, the discretized momentum equations are solved implicitly using the old time pressure to obtain an intermediate velocity field ($\boldsymbol{u}_P^*$). A backward Euler scheme is used for the discretization of the time derivative term

$$\mathbf{u}_P^* = \mathbf{H}[\mathbf{u}^*]_P - D_P(\nabla_{\mathrm{d}}P^{n-1})_P + \frac{(\rho\mathbf{u})^{n-1}}{A_P^{\mathbf{u}}\delta t} \tag{13}$$

where $\mathbf{H}$ is a linear operator resulting from the discretization of convection and diffusion terms, and D_P is defined as follows for the collocated grid:

$$D_P = V_P/A_P^{\boldsymbol{u}} \tag{14}$$

The intermediate velocity field does not satisfy mass continuity and needs to be corrected using the continuity equation as a constraint. In the first corrector step, a new velocity field, $\boldsymbol{u}^{**}$, and a new pressure field, P^*, are sought. The discretized momentum equation at this step is written as

$$\mathbf{u}_P^{**} = \mathbf{H}[\mathbf{u}^*]_P - D_P(\nabla_{\mathrm{d}}P^*)_P + \frac{(\rho\mathbf{u})_P^{n-1}}{A_p^{\mathbf{u}}\delta t} \tag{15}$$

Equation (13) is subtracted from Equation (15), leading to the velocity correction term

$$\mathbf{u}_P^{**} = \mathbf{u}_P^* - D_P(\nabla_{\mathrm{d}}P')_P \tag{16}$$

If the pressure field depends on the density field, such as in high-speed flows or in cavitating flows, density field needs to be corrected as follows:

$$\rho_P^* = \rho_P^{n-1} + \rho_P', \quad \rho_P' = C_\rho P_P' \tag{17}$$

C_ρ is the pressure–density coupling scheme, which is discussed in the next section. The discretized continuity equation written for the new velocity field and density field reads the following:

$$\frac{\rho_P^* - \rho_P^{n-1}}{\delta t} V_P + \Delta[\rho^* u^{**} \cdot \mathbf{n}S_{\mathrm{cf}}]_P = 0 \tag{18}$$

Inclusion of the corrected velocity field, Equation (16) and density field, Equation (17), transforms the above discretized continuity equation into a pressure-correction equation to be solved in the first corrector step

$$\frac{C_\rho P_P'}{\delta t} V_P - \Delta[\rho^{n-1}D(\nabla_{\mathrm{d}}P') \cdot \mathbf{n}S_{\mathrm{cf}}]_P + \Delta[C_\rho P' U^*]_P = -\Delta[\rho^{n-1}U^*]_P \tag{19}$$

When Equation (13) is subtracted from Equation (16), the terms containing operator **H** is lost. Hence, a second corrector step is needed to satisfy the mass conservation. In the second corrector step a new velocity field, $\mathbf{u}_P^{***}$, and a new pressure field, P^{**}, are sought. The discretized momentum equation at this step is written as

$$\mathbf{u}_P^{***} = \mathbf{H}[\mathbf{u}^{**}]_P - D_P(\nabla_d P^{**})_P + \frac{(\rho\mathbf{u})_P^{n-1}}{A_P^{\mathbf{u}}\delta t} \tag{20}$$

Then, Equation (15) is subtracted from Equation (20), leading to the following correction terms:

$$\mathbf{u}_P^{***} = \mathbf{u}_P^{**} + H[\mathbf{u}^{**} - \mathbf{u}^{*}]_P - D_P(\nabla_d P'')_P \tag{21}$$

Correspondingly, the density field needs to be corrected at this step also as follows:

$$\rho_P^{**} = \rho_P^{*} + \rho_P'' = \rho_P^{n-1} + \rho_P' + \rho_P'' \tag{22}$$

Inclusion of the corrected velocity field, Equation (21) and density field, Equation (22), transform the discretized continuity equation into a pressure-correction equation to be solved in the second corrector step

$$\frac{C_\rho P_P''}{\delta t} V_P - \Delta[\rho^* D(\nabla_d P'') \cdot \boldsymbol{n} S_{cf}]_P + \Delta[C_\rho P'' U^{**}]_P$$
$$= -\Delta[\rho^* U^{**}]_P - \Delta[\rho^* \mathbf{H}[\mathbf{u}^{**} - \mathbf{u}^{*}] \cdot \mathbf{n} S_{cf}]_P \tag{23}$$

Issa [26] has shown that addition of each corrector step increases the accuracy by order of one in time. We have found that, instead of adding an additional corrector step, repeating the first corrector and second corrector step one more time improves the fidelity of the time-dependent computation, such as the vortex shedding behind a cylinder and the associated Strouhal number, as presented in Reference [15]. Additionally, since the splitting error depends on time-step size, smaller time-steps are needed for time-accurate computations.

Oliveria and Issa [31] have discussed the coupling of temperature equation to the PISO algorithm for buoyancy-driven flows. Their study has shown that the PISO algorithm is amenable to different arrangements in the operator-splitting procedure. An improved method is developed to handle the strong coupling of velocity and temperature in buoyancy-driven flows. Similarly, for turbulent cavitating flow computations, special attention is also needed to couple the cavitation model and the turbulence model equations in the operator splitting procedure. The sequence of operations in PISO for turbulent cavitating flow computations is described below:

1. Predictor step: solve the discretized momentum equation, Equation (13), implicitly.
2. Compute C_ρ needed for pressure–density coupling.
3. First corrector step: solve the convective–diffusive pressure-correction equation, Equation (19), implicitly.
4. Correct the velocity and pressure field.
5. Solve implicitly the discretized scalar equations for α_L, k and ε, resulting from cavitation and turbulence models, using the corrected velocity and pressure field.

6. Compute the density field and turbulent viscosity fields.
7. Compute C_ρ needed for pressure–density coupling.
8. Second corrector step: solve the convective–diffusive pressure correction equation, Equation (23), implicitly.
9. Correct the velocity and pressure field.
10. Solve explicitly the discretized scalar equations for α_L, k and ε, resulting from cavitation and turbulence models, using the corrected velocity and pressure field (no need for a matrix solver).
11. Compute the density and turbulent viscosity field.
12. Go to Step 2 and repeat the steps one more time to enhance the coupling.
13. Proceed to the next time step.

As explained in Reference [14], the density at the cell face is upwinded based on a single point extrapolation, both in the discretized momentum and pressure-correction equations, to enhance mass and momentum conservation in regions of sharp density gradients.

4.1. The issue of speed of sound definition

In Reference [14], we have discussed the importance of pressure–density coupling for cavitating flow computations with pressure-based algorithms. The discussion still holds for the present pressure-based operator-splitting algorithm. For steady flow computations, the pressure–density coupling scheme only affects the convergence path. The final solution is independent of the choice because of the nature of pressure-correction. However, for unsteady flow computations the choice of pressure–density coupling becomes critical, since it relates the propagation of information from the cavitating region to the rest of the domain. The pressure–density coupling term C_ρ is a measure of the isentropic speed of sound. The relation is given as follows:

$$\rho' = C_\rho P', \quad C_\rho = \left(\frac{\partial \rho}{\partial P}\right)_S = \frac{1}{c^2} \tag{24}$$

where c is the speed of sound.

In high-speed flows, the exact form of the speed of sound can be computed easily from the equation of state. However, in cavitating flows, computation of the speed of sound is not an easy task. Each transport equation-based cavitation model defines a different speed of sound as a result of the complex fluid physics. In the literature, there are theoretical studies on defining the speed of sound in multiphase flows [32]. One-dimensional assumptions and certain limitations are typical in these studies. On the other hand, the practical implementation of the fundamental definition of speed of sound as given in Equation (24) depends on the path to compute the partial derivative. The computation of the speed of sound in cavitating flows is an open question.

In this study, two different definitions for the speed of sound is investigated in the pressure–density coupling scheme. The first one has been proposed in Reference [14] for steady flow computations because of its good computational stability characteristics. It is written as

$$C_\rho = \left(\frac{\partial \rho}{\partial P}\right)_S = \frac{1}{c^2} \approx C(1 - \alpha_L) \tag{25}$$

where C is an arbitrary constant and a value of 4 is adopted. The above form is referred to as SoS-1 hereinafter.

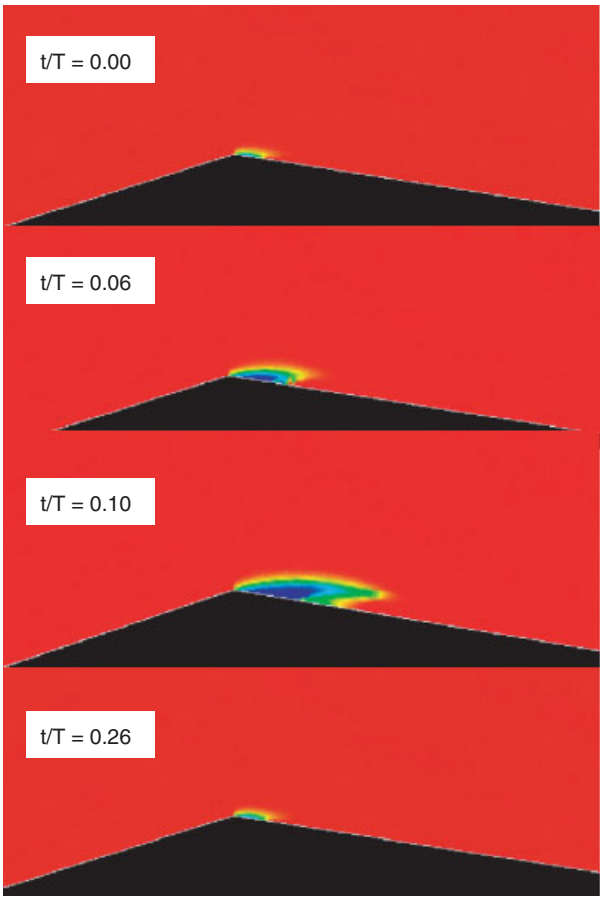

Plate 1. Cavity shapes obtained from the computation adopting Model-2 [13].

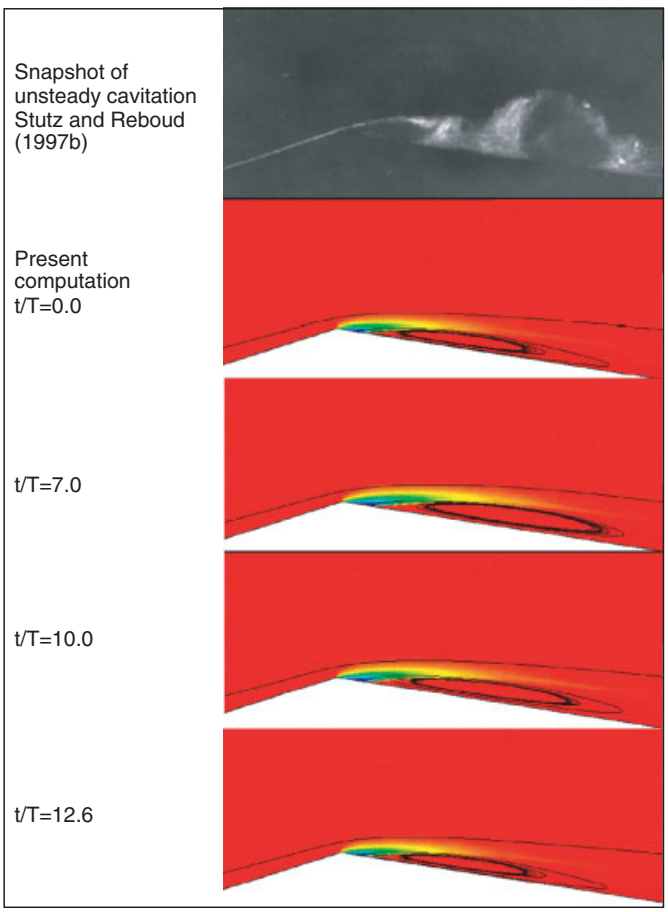

Plate 2. Cavity shapes and the recirculation zone during the instability cycle. Geometry is Nozzle-1. The new interfacial dynamics cavitation model is used. The cavitation number is 1.98 based on time-averaged quantities. The experimental photo is reproduced from Reference [8] with the permission of Springer–Verlag.

The second one is based on an approximation made to the fundamental definition of speed of sound, Equation (24), with the path to compute the partial derivative $\partial\rho/\partial P$ taken to be the body fitted curvilinear co-ordinate (ξ) that is aligned with the mean flow direction. This second definition is referred to as SoS-2 hereinafter, and it is given as follows:

$$C_\rho = \left(\frac{\partial\rho}{\partial P}\right)_S \approx \left(\frac{\Delta\rho}{\Delta P}\right)_\xi = \left|\frac{\rho_{i+1} - \rho_{i-1}}{P_{i+1} - P_{i-1}}\right| \tag{26}$$

The partial derivative is computed based on central differencing of the neighbouring nodes. The absolute sign is introduced to make sure a positive value is computed.

4.2. *Boundary conditions*

The velocity components, volume fractions and turbulence quantities are specified at the inlet boundary. At the outlet, a zero gradient condition is imposed for velocity and volume fraction. For unsteady flow computations, a zero gradient condition for pressure-correction causes difficulties because the global mass conservation condition involves the time derivative terms of density; hence, the pressure is specified on the outlet boundary for unsteady flow computations [25]. The outlet boundary is placed far away from the cavitating region of interest. This type of outlet boundary condition does not require a global mass conservation condition since the pressure correction is exactly zero because of the specified pressure.

5. RESULTS AND DISCUSSION

Stutz and Reboud [7–9] have performed a series of experiments to study cavitating flow structure in convergent–divergent nozzles. Time-averaged velocity and vapour volume fraction profiles within the cavity and qualitative description of the cavity behaviour have been presented in these studies. Stutz and Reboud [8, 9] have studied unsteady cavitation formed in a different convergent–divergent nozzle. In this particular geometry, the convergent angle is 18° and the divergent part angle is 8°. The throat height is 34.3 mm. Cavitation formed in this nozzle is described as unsteady and vapour cloud shedding is typical. The computational domain and the imposed boundary conditions are shown in Figure 1. This particular geometry is referred to as Nozzle-1 hereinafter.

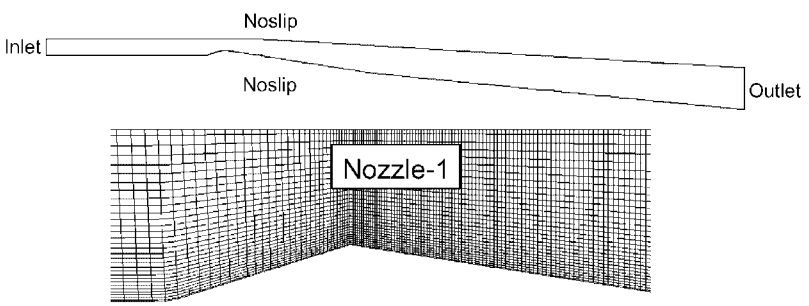

Figure 1. Nozzle-1, computational domain and the imposed boundary conditions.

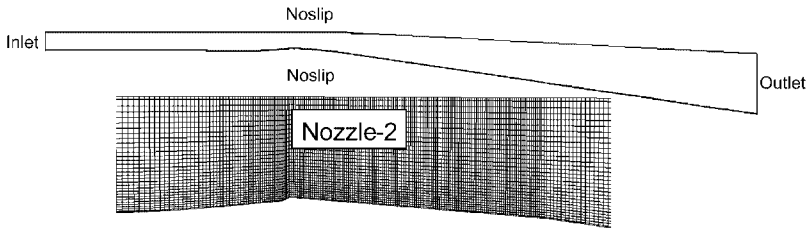

Figure 2. Nozzle-2, computational domain and the imposed boundary conditions.

Stutz and Reboud [7] have also studied stable sheet cavitation formed in a convergent–divergent nozzle. The angle of the convergent part is 4.3° and that of the divergent part is 4°. The throat height is 43.7mm. This geometry is shown in Figure 2 and is referred to as Nozzle-2 hereinafter. Reboud *et al.* [33] have conducted a computational study to compare with their experimental findings. In their study, an arbitrary barotropic equation [34, 35] is adopted for cavitation modelling. They have indicated that the use of the original k–ε turbulence model [17] leads to a steady-state cavity with no re-entrant jet formed in the closure region, apparently because of high turbulent viscosity induced by the turbulence model. They have modelled the unsteadiness by empirical reduction of the turbulence dissipative terms in the cavitating regions.

The experiments indicate unsteady cavitation with clouds of vapour in Nozzle-1 [8, 9], and stable sheet cavitation in Nozzle-2 [7]. Compared to Nozzle-1, Nozzle-2 has less confinement in the throat section and modest convergent–divergent angles. The original k–ε turbulence model [17] is adopted here with no modification. It should be mentioned that the experiments, detailed in References [7–9], present only the time-averaged velocity and void fraction profiles within the cavity. The unsteadiness observed by them is mostly described qualitatively.

5.1. Implications of the speed of sound definition

In the incompressible liquid phase, the speed of information propagation is infinite and any disturbance, generated in the cavitating region, is instantaneously conveyed to the rest of the flow domain. We have proposed two different approximations as SoS-1 and SoS-2, to shed light on the effect of speed of sound definition for the cavitating region. Figure 3 shows time evolution of pressure at a point close to the inlet boundary of Nozzle-1. The new interfacial dynamics cavitation model [16] is used. On the left of Figure 3 are the results based on SoS-1, and on the right are the results based on SoS-2. The significant impact of the choice of speed of sound definition is clear. Apparently, SoS-1 does not produce the correct behaviour, because the periodic behaviour weakens as the cavitation number is decreased. On the other hand, SoS-2 exhibits qualitatively correct behaviours. At higher cavitation numbers, the flow goes to a steady solution after an initial transient, and as the cavitation number is lowered a periodic behaviour emerges. The origin of this unsteady behaviour is discussed in more details in the coming section.

As discussed in Part-1, different cavitation models have produced satisfactory pressure distributions in the case of steady flow computations. Differences are mainly in density profiles at the closure region, likely caused by the variations in compressibility characteristics between different cavitation models. The present unsteady flow simulations support strongly this view

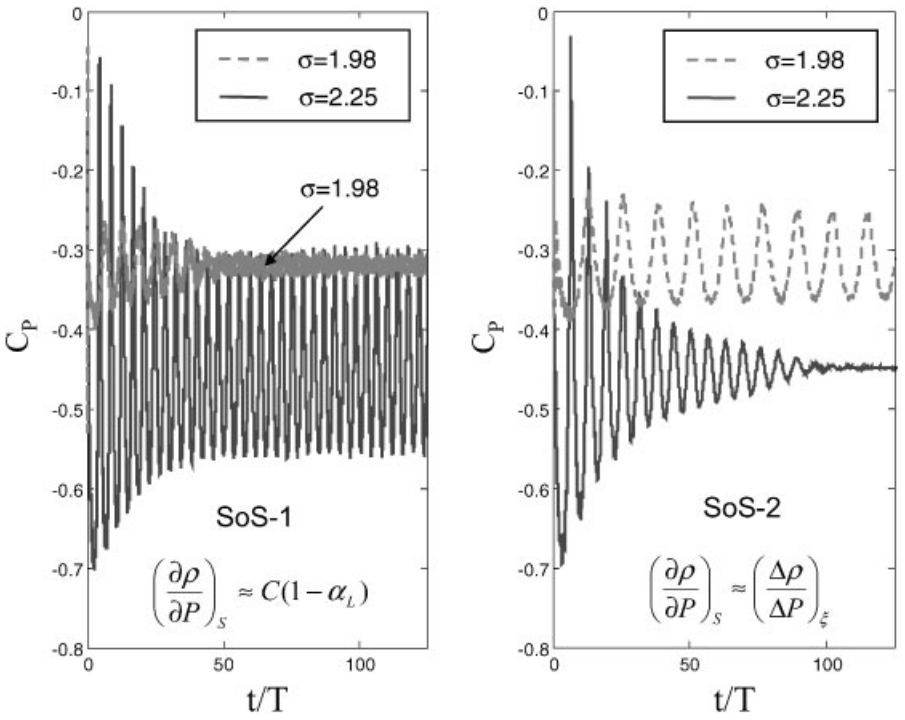

Figure 3. The impact of the speed of sound definition on time-dependent behaviour. The new interfacial dynamics cavitation model is used. Geometry is Nozzle-1.

as shown in Figure 4. This figure compares time-dependent behaviours of the new interfacial dynamics-based cavitation model and Model-2 based on the same speed of sound definition, SoS-2. The oscillations of the upstream pressure are considerably different. Model-2 [13] does not produce the unsteady behaviour observed in the experiments of Stutz and Reboud [8, 9]. As shown in Plate 1, the cavity completely collapses and then reappears during its cycle, in contrast to a self-oscillating mean cavity observed in the experiments. The results of the new interfacial dynamics-based cavitation model indicate a sustained cavity; as the cavitation number is decreased a quasi-periodic behaviour with mean cavity emerges.

We have investigated the speed of sound definition for computations of unsteady cavitation formed in Nozzle-1, based on the experiments of Stutz and Reboud [8, 9]. As already mentioned, Stutz and Reboud [7] have reported steady-state cavity dynamics in their experiments on sheet cavitation formed in Nozzle-2. Figure 5shows the time evolution of pressure at a point close to the inlet boundary of Nozzle-2. Both the new interfacial dynamics-based cavitation model and Model-2 are used. As seen on the left plot of Figure 5, both models exhibit unsteady behaviour if SoS-1 is adopted. This is obviously not consistent with the quasi-steady cavity behaviour observed in the experiments [7]. But if SoS-2 is adopted, the correct stable behaviour is captured by both cavitation models Based on these numerical tests, it seems that SoS-2, gives qualitatively more correct time-dependent behaviours. This test study, regarding the speed of sound definition and cavitation models, has shown that the

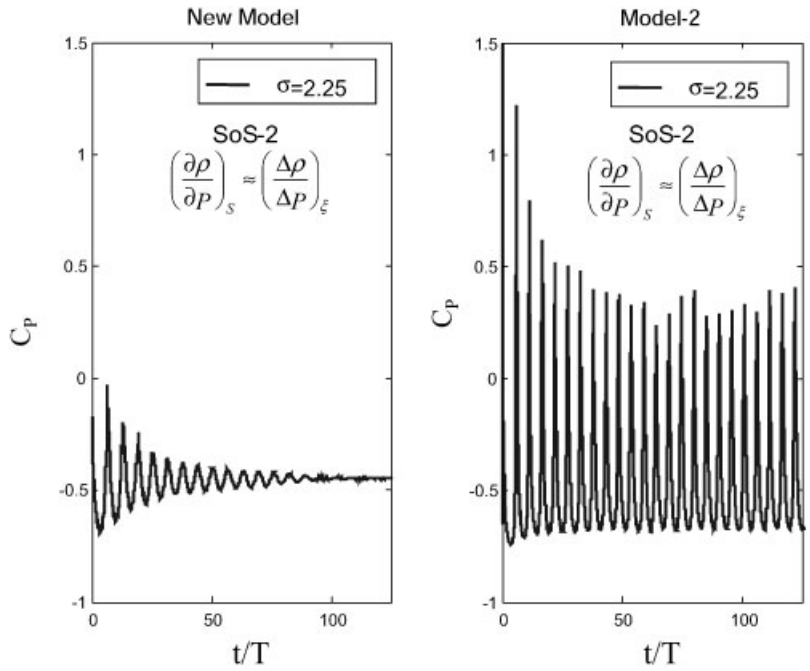

Figure 4. Comparison of the time-dependent behaviour of different cavitation models. Geometry is Nozzle-1.

new interfacial dynamics cavitation model [16] along with SoS-2 definition can produce the correct unsteady behaviour. We will further employ this approach to investigate other cases, as presented below.

5.2. *Cavitation instability (Auto-oscillations)*

Plate 2 shows the shapes of the cavity during the auto-oscillation cycle observed in Nozzle-1. The computations have captured a mean cavity and a recirculation zone. Snapshot of the unsteady cavitation [8] is also included to assess the present findings. The main cavity body is in good agreement with the experiment, as shown in Plate 2. However, the experimental photograph indicates a large-scale structure that rolls up and sheds clouds of vapour, which is not captured in the present computations. Kubota *et al.* [6] have associated the cloud cavitation motion with the large-scale velocity. The reason that the cloud cavitation is not captured in the present results may be due to the adoption of the original k–ε turbulence model [17], which induces high turbulent viscosities in regions of turbulence production. The typical Strouhal number of the shedding of cloud cavitation is found to be about 0.30 in various studies [2, 8, 9]. In the present results, no shedding of cloud cavitation is captured; hence, the Strouhal number is not in agreement with the above value. The reduced frequency of the auto-oscillations of the cavity, fc/U, based on characteristic length and the reference velocity is computed as 0.08 based on the cavity cycle shown in Plate 2. This number is in agreement with the reduced frequency (0.07) of the cavitation surge

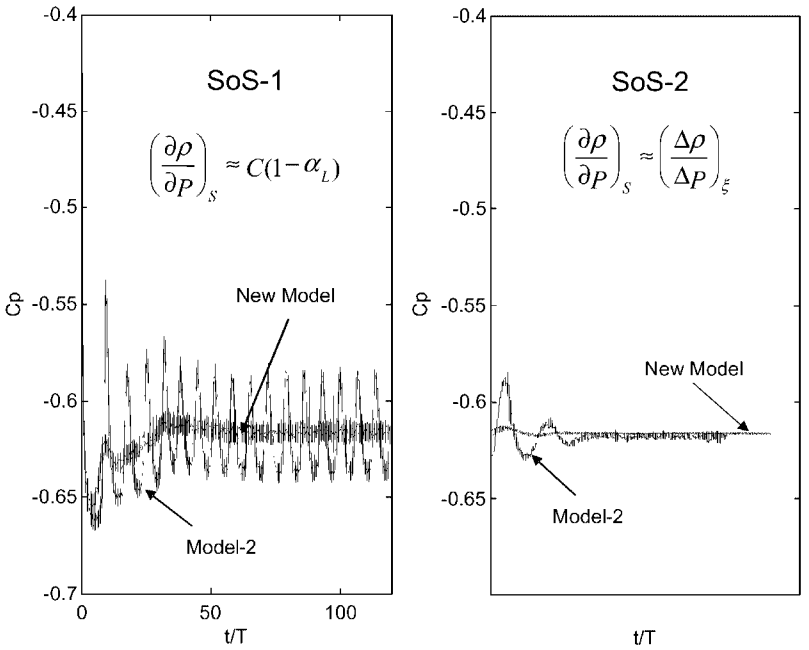

Figure 5. The impact of the speed of sound definition on time-dependent behaviour. Geometry is Nozzle-2. The cavitation number is 0.67.

instability on a propeller, presented in Reference [5], where no periodic shedding of cloud cavitation is observed. As mentioned by Duttweiler and Brennen [5], the reduced frequency observed in their experiments are in accordance with other experimental cavitation studies on two-dimensional hydrofoils. It appears that there are two dominant scales related to the observed unsteadiness, large-scale motion responsible for vortex shedding and cloud cavitation, and smaller scale motion for attached cavity. The Strouhal numbers associated with these two regimes are different in magnitudes. The present modelling strategy, adopting the original k–ε turbulence model, seems to capture the small-scale transient behaviour more easily.

Figure 6 shows the quasi-periodic oscillation of the upstream pressure in Nozzle-1. The similar behaviour of the far field pressure is reported as cavitation surge in Reference [5] for a cavitating propeller in a water tunnel. As previously shown in the right plot of Figure 3, this periodic behaviour emerges as the cavitation number is decreased.

Callenaere *et al.* [2], have studied the effects of confinement in a venturi-type test section and they have found that the auto-oscillations develop as the confinement is increased, indicating the prominent role of pressure gradient along the channel. In their study, the pressure gradient has also been controlled by varying the divergent angle of the test section. The auto-oscillation disappears as the divergent angle is decreased. If the results obtained from two nozzles (Nozzle-1 and Nozzle-2) are investigated in a collective approach, the prominent role of the pressure gradient in generating the auto-oscillations can be clearly identified.

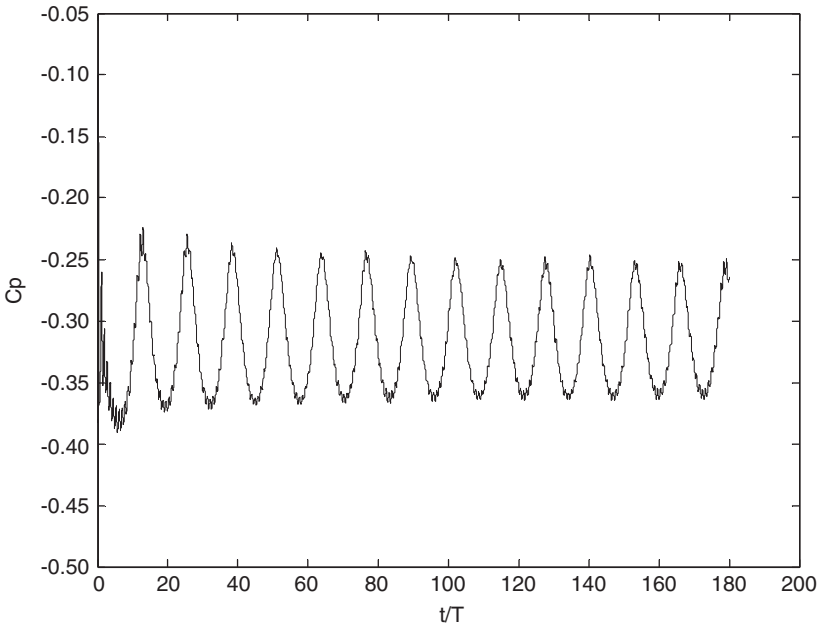

Figure 6. The quasi-periodic oscillation of the upstream pressure in Nozzle-1. The cavitation number is 1.98 based on time-averaged quantities.

To summarize, Nozzle-1 has a narrow throat section with large convergent–divergent angles, whereas Nozzle-2 has a wider throat section with smaller convergent–divergent angles; hence, the flow is less confined in the case of Nozzle-2. In Nozzle-1, the cavity incepts and grows in length and thickness contracting the effective area at the throat section, which leads to auto-oscillation of the cavity. However, in Nozzle-2 quasi-steady sheet cavitation is observed. Such characteristics of the present numerical simulations are consistent with the experimental observations of Callenaere *et al.* [2]. In Figure 7, the pressure along Nozzle-1 at half-way from the bottom to the top surface is plotted. Hence, it is representative of the pressure gradient acting along the nozzle. The pressure distributions for both minimum and maximum cavity are shown. It is clear that as the cavity grows the adverse pressure gradient gets stronger. This has two effects. First, the strong adverse pressure gradient enhances the recirculation zone. The second effect is on the mass transfer. Since the mass transfer terms of the new interfacial dynamics-based cavitation model are functions of the pressure difference, the interfacial velocities and the void fraction, condensation dominates as the cavity reaches its maximum size. As a result the cavity starts shrinking. When the cavity reaches its minimum size, evaporation dominates, leading to an expansion of the cavity. The process repeats itself quasi-periodically leading to the cavitation instability observed as auto-oscillations. From these arguments, it seems clear that the mass transfer, depending on the pressure distribution, interfacial velocities and void fraction, also plays a noticeable role in the observed cavitation instability.

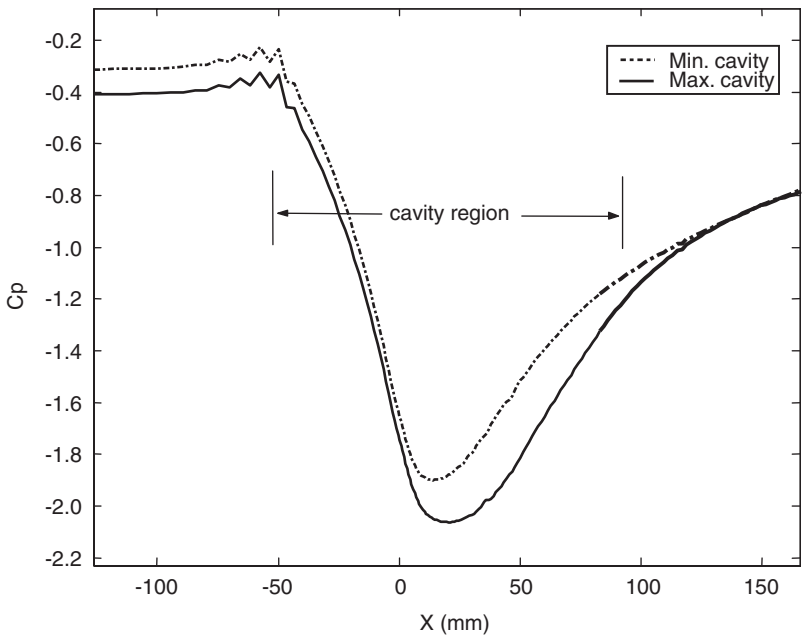

Figure 7. Pressure distribution along the nozzle at min and max cavity size.

5.3. *Two-phase flow structure*

Time-averaged velocity and vapour volume fraction profiles are compared with experimental data of Stutz and Reboud [7–9] to assess the results of Nozzle-1 and Nozzle-2 cases.

Figures 8 and 9 show the time-averaged velocity and vapour volume fraction profiles within the cavity formed in Nozzle-1. The boundary of the cavitating region is also included in Figure 8. The computations capture the main cavity body; however, the total time-averaged cavity boundary is not captured. Reasonable agreement is observed in the velocity profiles given in Figure 8, especially in the core of the reverse flow. The vapour volume fraction measured in the experiments shows high mixture content, which is typical in cloud cavitation. Although the computations do not match the experimental data quantitatively, the overall trends are agreeable.

Figures 10 and 11 show the velocity and vapour volume fraction profiles, respectively, within the cavity formed in Nozzle-2. Recall that a steady flow computation has been performed for this particular geometry and the corresponding results are documented in Part-1 [16]. Overall, the time-averaged results have noticeably improved the agreement with the time-averaged experimental data. The agreement in the reverse flow is improved as compared to the results based on steady flow computations [16].

The predicted vapour volume fraction profiles resulting from time-dependent computations also show improved agreement with the experiment. The disagreement is mainly in the reverse flow region. The computations indicate mostly liquid content, whereas the experimental results show a mixture flow. This also explains, in part, the disagreement of the velocity profiles in the reverse flow. The reverse mixture flow, observed in the experiments, has higher velocity

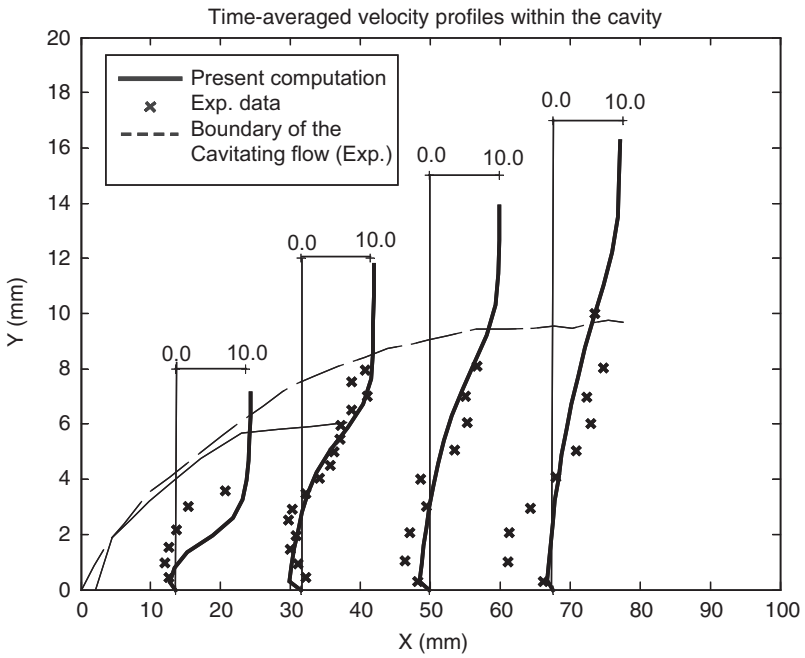

Figure 8. Time-averaged velocity profiles (u/U_{ref}) within the cavity formed in Nozzle-1. The vertical scale is the distance from the wall. Experimental data is from Reference [9]. The cavitation number is 1.98.

due to its lower density. However, the high density slows down the motion of the reverse flow, captured in the computations.

6. CONCLUSIONS

For time-dependent simulations of turbulent cavitating flows, a pressure-based operator-splitting algorithm (PISO) has been extended to improve the coupling of the cavitation and turbulence models, and to handle the large density ratio associated with cavitation. The implications of the compressibility effect, reflected via the local speed of sound definition in the two-phase mixture, have been investigated for time-dependent computations. Two approximations regarding the speed of sound definition in the two-phase mixture have been proposed. It is shown that the definition of local speed of sound of the two-phase mixture has significant impact on the unsteady behaviour captured in the simulations. Unlike steady flow computations presented in Part-1 of the present study [16], the cavitation model choice strongly impacts the prediction of unsteady behaviour.

Cavitation instability has been observed as auto-oscillations of the attached cavity formed in a convergent–divergent nozzle. The upstream pressure oscillates quasi-periodically in response to cavity oscillations. The reduced frequency of the auto-oscillations has been found to be in good agreement with the experimental value reported in Reference [5]. However, the high

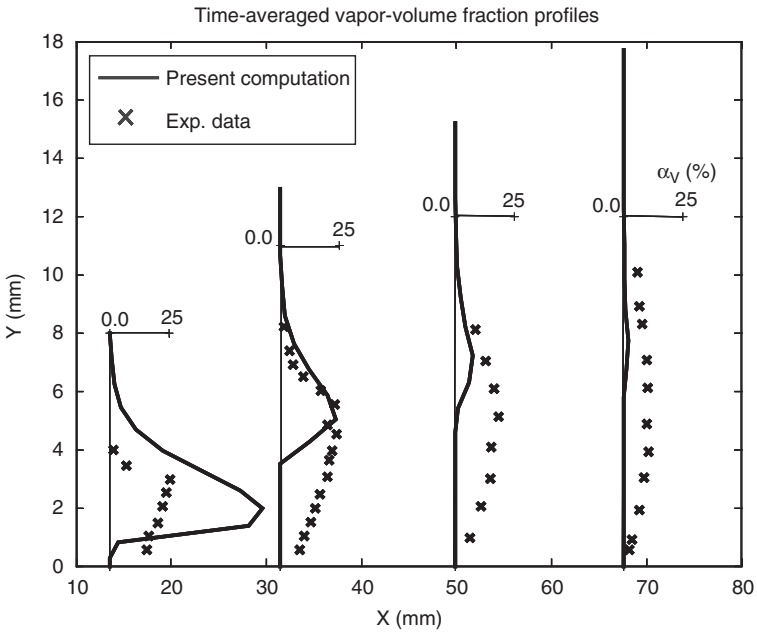

Figure 9. Vapor volume fraction profiles within the cavity formed in Nozzle-1. The vertical scale is the distance from the wall. Experimental data is from Reference [9]. The cavitation number is 1.98.

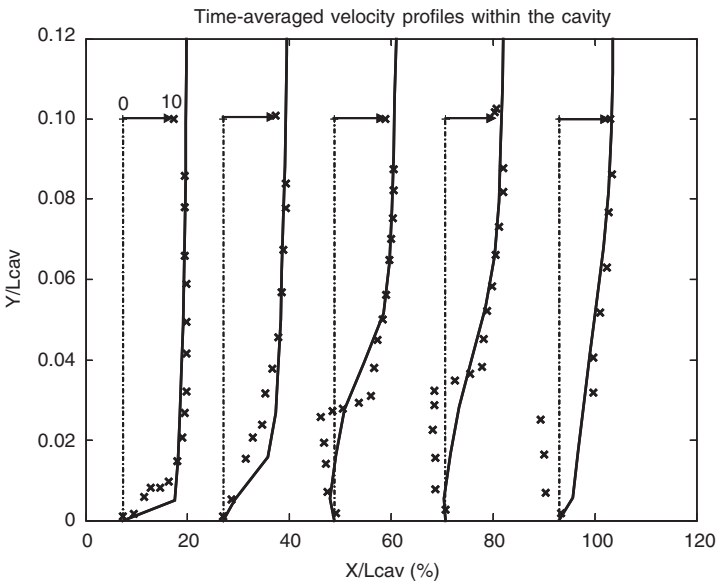

Figure 10. Time-averaged velocity profiles (u/U_{ref}) within the cavity formed in Nozzle-2. The vertical and horizontal scales are normalized by $L_{\text{cav}} = 80$ mm to be consistent with the experimental data. The vertical scale is the distance from the wall. Experimental data is from Reference [7]. The cavitation number is 0.67.

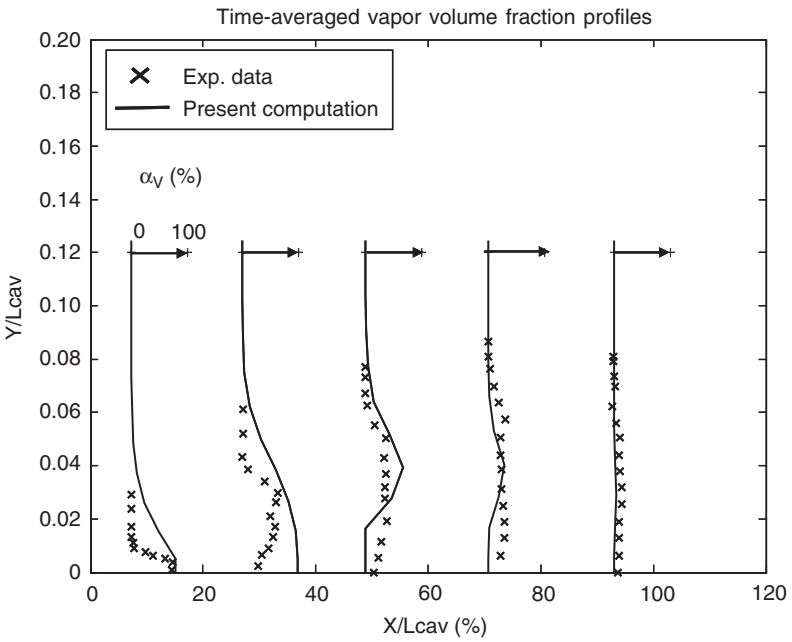

Figure 11. Time-averaged vapour volume fraction profiles within the cavity formed in Nozzle-2. The vertical and horizontal scales are normalized by $L_{cav} = 80$ mm to be consistent with the experimental data. The vertical scale is the distance from the wall. Experimental data is from Reference [7]. The cavitation number is 0.67.

frequency of the shedding of cloud cavitation is not captured due to limitations of the original k–ε model. The effect of pressure gradient on the cavitation instability has been highlighted by considering two convergent–divergent nozzles with different degree of geometric confinement around the cavitation region. The adverse pressure gradient is stronger at maximum cavity size. Owing to changes in the local flow quantities, the mass transfer rates are different during the cavity oscillations. Hence, the cavitation instability is affected not only through the reverse flow due to adverse pressure gradients, as reported in Reference [2], but also through the mass transfer process. Furthermore, the time-dependent computations have produced improved predictions of velocity and void fraction distributions as compared to steady flow computations presented in Part-1 of the present study [16].

To enhance our computational capabilities, future work is needed in the following areas:

- The speed of sound definition in cavitating regions remains an open question. Each transport equation-based cavitation model defines a different relation, which is complex.
- The original k–ε model has limitations to capture cloud cavitation. The model induces high turbulent viscosity, which dampens the large-scale velocity structures.
- Interface tracking capabilities for turbulent two-phase flows. One needs to consider the body-fitted curvilinear co-ordinates to handle cavitating flow problems in complex geometries.

ACKNOWLEDGEMENTS

This study has been supported partially by the NASA URETI programme and the U.S. Air Force. We appreciate B. Stutz and J. L. Reboud for the interactions regarding their experimental study.

REFERENCES

1. Knapp RT, Daily JW, Hammitt FG. *Cavitation*. McGraw-Hill: New York, 1970.
2. Callenaere M, Franc JP, Michel JM, Riondet M. The cavitation instability induced by the development of a re-entrant jet. *Journal of Fluid Mechanics* 2001; **444**:223.
3. Watanabe S, Tsujimoto Y, Franc JP, Michel JM. Linear analyses of cavitation instabilities. *Proceedings of the 3rd International Symposium on Cavitation*, Grenoble, France, 1998.
4. Franc JP. Partial cavity instabilities and re-entrant jet. CAV2001, *Proceedings of the 4th International Symposium on Cavitation*, Pasadena, CA, U.S.A. CAV2001:lecture.002, 2001, http://cav2001.library.caltech.edu
5. Duttweiler ME, Brennen CE. Surge instability on a cavitating propeller. *Journal of Fluid Mechanics* 2002; **458**:133.
6. Kubota A, Kato H, Yamaguchi H, Maeda M. Unsteady structure measurement of cloud cavitation on a foil section using conditional sampling technique. *Journal of Fluids Engineering* 1989; **111**:204.
7. Stutz B, Reboud JL. Two-phase flow structure of sheet cavitation. *Physics of Fluids* 1997; **9**(12):3678.
8. Stutz B, Reboud JL. Experiments on unsteady cavitation. *Experiments in Fluids* 1997; **22**:191.
9. Stutz B, Reboud JL. Measurements within unsteady cavitation. *Experiments in Fluids* 2000; **29**:545.
10. Reisman GE, Wang YC, Brennen CE. Observations of shock waves in cloud cavitation. *Journal of Fluid Mechanics* 1998; **355**:255.
11. Ahuja V, Hosangadi A, Arunajatesan S. Simulations of cavitating flows using hybrid unstructured meshes. *Journal of Fluids Engineering* 2001; **123**:331.
12. Merkle CL, Feng JZ, Buelow PEO. Computational modelling of the dynamics of sheet cavitation. *Proceedings of the 3rd International Symposium on Cavitation*, Grenoble, France, 1998.
13. Kunz RF, Boger DA, Stinebring DR, Chyczewski TS, Lindau JW, Gibeling HJ, Venkateswaran S, Govindan TR. A preconditioned Navier–Stokes method for two-phase flows with application to cavitation prediction. *Computers and Fluids* 2000; **29**:849.
14. Senocak I, Shyy W. A pressure-based method for turbulent cavitating flow computations. *Journal of Computational Physics* 2002; **176**:363.
15. Senocak I. Computational methodology for the simulation of turbulent cavitating flows. *Ph.D. Thesis*, University of Florida, Gainesville, FL, U.S.A., 2002, http://purl.fcla.edu/fcla/etd/UFE1001181
16. Senocak I, Shyy W. Interfacial dynamics-based modelling of turbulent cavitating flows, Part-1: Model development and steady-state computations. *International Journal for Numerical Methods in Fluids* 2004; **44**:975–995.
17. Jones WP, Launder BE. The prediction of laminarization with a two-equation model of turbulence. *International Journal of Heat and Mass Transfer* 1972; **15**:301.
18. Launder BE, Spalding DB. The numerical computation of turbulent flows. *Computer Methods in Applied Mechanics and Engineering* 1974; **3**:269.
19. Shyy W. *Computational Modeling for Fluid Flow and Interfacial Transport*. Elsevier: Amsterdam, The Netherlands (revised printing 1997).
20. Shyy W, Thakur SS, Ouyang H, Liu J, Blosch E. *Computational Techniques for Complex Transport Phenomena*. Cambridge University Press: New York, 1997.
21. Brackbill JU, Kothe DB, Zemach C. A continuum method for modelling surface tension. *Journal of Computational Physics* 1992; **100**:335.
22. Francois M. A study of the volume of fluid method for moving boundary problems. *M.Sc. Thesis*, Embry Riddle Aeronautical University, Daytona Beach, FL, U.S.A., 1998.
23. Rajkumar V, Senocak I, Wu J, Shyy W. Sensitivity evaluation of a transport-based turbulent cavitation model. *Journal of Fluids Engineering* 2003; **125**(3):447.
24. Shyy W, Udaykumar HS, Rao MM, Smith RW. *Computational Fluid Dynamics with Moving Boundaries*. Taylor & Francis: Washington, DC, 1996 (revised printing 1997, 1998 & 2001).
25. Patankar SV. *Numerical Heat Transfer and Fluid Flow*. Hemisphere: Washington, DC, 1980.
26. Issa RI. Solution of the implicitly discretized fluid flow equations by operator-splitting. *Journal of Computational Physics* 1985; **62**:40.
27. Braaten ME, Shyy W. A study of pressure correction methods with multigrid for viscous flow calculations in non-orthogonal curvilinear co-ordinates. *Numerical Heat Transfer* 1987; **11**:417.
28. Bressloff NW. A parallel pressure implicit splitting of operators algorithm applied to flows at all speeds. *International Journal for Numerical Methods in Fluids* 2001; **36**:497.

29. Thakur SS, Wright JF, Shyy W. STREAM: A computational fluid dynamics and heat transfer Navier–Stokes solver: Theory and applications. Streamline Numerics, Inc. and Computational Thermo-Fluids Laboratory, Department of Mechanical and Aerospace Engineering Technical Report, Gainesville, Florida, 2002.
30. Moukalled F, Darwish M. A unified formulation of the segregated class of algorithms for fluid flow at all speeds. *Numerical Heat Transfer Part B-Fundamentals* 2000; **37**:103.
31. Oliveira PJ, Issa RI. An improved PISO algorithm for the computation of buoyancy-driven flows. *Numerical Heat Transfer Part B-Fundamentals* 2001; **40**:473.
32. Wallis GB. *One-dimensional Two-phase Flow*. McGraw-Hill: New York, 1969.
33. Reboud JL, Stutz B, Coutier O. Two-phase flow structure of cavitation: experiment and modelling of unsteady effects. *Proceedings of the 3rd International Symposium on Cavitation*, Grenoble, France, 1998.
34. Delannoy Y, Kueny JL. Cavity flow predictions based on the Euler equations. *ASME Cavitation and Multiphase Flow Forum*, ASME-FED vol. **98**: pp 153–158. 1990.
35. Reboud JL, Delannoy Y. Two-phase flow modelling of unsteady cavitation. *Proceedings of the 2nd International Symposium on Cavitation*, Tokyo, Japan, 1994.

